

AN ENHANCED STATISTICAL-AI NUMERICAL METHOD FOR MODELING TRACE GAS DISPERSION IN ATMOSPHERIC FLOWS

AMINE AJDOUR^{1,2}, HOURIA BOUZGHIBA¹, BRAHIM YDIR², ABDERRAHMANE MENDYL³, ANAS ADNANE^{2,4}, JAMAL CHAOUFI², GÁBOR GÉCZI⁵, RADOUANE LEGHRIB²

¹*Doctoral School of Environmental Sciences, Hungarian University of Agriculture and Life Sciences, 2100, Páter Károly utca 1, Hungary*

²*Laboratory of Materials, Signals, Systems and Physical Modeling, Physics Department, Faculty of Sciences, Ibn Zohr University, Agadir, Morocco*

³*Department of Meteorology, Institute of Geography and Earth Sciences, ELTE Eötvös Loránd University, H-1117 Budapest, Hungary*

⁴*General Directorate of Meteorology, Face Préfecture Hay Hassani, B.P. 8106 Casa-Oasis, Casablanca, Morocco*

⁵*Institute of Environmental Sciences, Department of Environmental Analysis and Environmental Technology, Hungarian University of Agriculture and Life Sciences, 2100, Páter Károly utca 1, Hungary*

E-mail : amine.ajdour@edu.uiz.ac.ma, ajdour@gmail.com

Received

Abstract. Addressing the limitations of traditional air pollution monitoring, this study leverages advanced computational techniques to enhance Modeling Trace Gas Dispersion in Atmospheric Flows. By integrating multivariate analysis with statistical and AI models, we aim to bridge gaps in spatial coverage and improve predictive accuracy. The methodology involves three steps: (i) identifying relationships between atmospheric pollutants and local meteorological factors using multivariate analysis, including correlations and principal component analysis (PCA); (ii) enhancing O₃ and NO₂ prediction accuracy with statistical and AI models like Multiple Linear Regression (MLR) and Two-Layer Feed-Forward Neural Networks (TLFFN), validated over 2014, 2016, and 2018; (iii) predicting O₃ and NO₂ levels across sixteen districts using data from seven sites with MLR and TLFFN models, and mapping using QGIS with inverse distance weighted (IDW) interpolation for spatial predictions. Results show that, according to PCA, O₃ is influenced by temperature, wind speed, and sulfur dioxide, while NO₂ is affected by pressure and CO. The MLR model, combined with QGIS-IDW, effectively generates ozone maps, aiding decision-makers. Using QGIS-IDW and TLFFN helps refine NO₂ data and reconstruct missing information, which is beneficial for atmospheric pollution modeling. Geospatial datasets and AI-GIS methods effectively integrate air quality improvements into urban planning.

Key words: Numerical Method, Atmospheric Flows, Spatio-Temporal Optimization, Multivariate Analysis, Inverse Distance Weighting, Artificial Intelligence.

1. INTRODUCTION

1.1. Research Background

As urbanization and industrialization persist in their global expansion, the complexities of atmospheric dynamics and pollutant dispersion necessitate a comprehensive understanding of the interaction between meteorological conditions and air quality [1,2]. Pollution monitoring through measurement stations is not always available, thus making modeling an essential tool. Traditional forecasting models, such as deterministic models, often encounter issues regarding result accuracy [3,4]. In other cases, they frequently fail to capture the intricate relationships between various atmospheric variables, resulting in inaccuracies and limitations in forecasting capabilities. Recently, there has been a trend towards adopting Artificial Intelligence (AI) models due to their accuracy and speed in delivering results [5–7]. The emergence of AI technologies has revolutionized pollution forecasting by enabling the development of sophisticated predictive algorithms capable of real-time learning from vast datasets. AI models can adapt to changing atmospheric conditions, enhancing their forecasting capabilities and reliability. Despite this, these models suffer from limitations such as the quality of input data, data availability, data imbalance, and sometimes interpretability [8,9], which necessitate careful data processing steps.

Multivariate analysis is a powerful approach for exploring complex relationships between several variables. Employing statistical and mathematical techniques explores the interactions between variables and identifies underlying patterns [10,11]. This process begins with collecting data on multiple variables and choosing the appropriate analysis method according to specific objectives. The data are pre-processed before the analysis method is applied to ensure their quality and relevance. These results can then be validated and used to inform decision-making, improve predictive models, or guide new avenues of research [12,13]. Overall, multivariate analysis offers a robust framework for exploring and exploiting the information contained in multidimensional datasets, providing valuable insights across various application domains [14]. Synthesizing complex information into simpler, multivariate analysis optimizes the inputs of statistical and artificial intelligence models, leading to more accurate predictions and can be exploited to create artificial stations [7,15].

Setting up artificial stations to predict air pollution at different sites using optimized statistical models and artificial intelligence (AI) involves a multi-faceted

approach that exploits state-of-the-art technologies to monitor and remediate air pollution levels [16]. Through the integration of statistical techniques and artificial intelligence algorithms, these stations can effectively forecast pollution patterns, locate sources, and generate pollution maps [15]. Air pollution mapping through interpolation methods, facilitated by Geographic Information Systems (GIS) platforms like ArcGIS or QGIS, offers a powerful approach to assessing air quality across vast regions with limited monitoring data [17]. By applying spatial interpolation techniques such as kriging, Inverse Distance Weighting (IDW), or spline interpolation, these models extrapolate pollution levels between discrete measurement points to create continuous representations of surface air pollution quality. GIS approaches can generate high-resolution maps depicting spatial variations in pollutant concentrations by integrating data from monitoring stations, satellite observations, and atmospheric models. These maps are valuable for policymakers, urban planners, and public health officials.

1.2. Related Work

Several studies are interested in analyzing the complex relationship between air quality and meteorological variables using various methods such as sensor data analysis, numerical weather prediction models to simulate realistic meteorological data, and employing time-lagged convergent cross-analysis to uncover causal relationships. Additionally, some studies utilize Bayesian network models or correlation analysis. The cumulative findings highlight the multifaceted relationship between meteorological variables, air quality, and public health outcomes. Wind direction emerges as an immediate influencer on air quality, while temperature's impact is observed to be delayed. Understanding these dynamics provides crucial insights for environmental management and the development of effective mitigation strategies. Factors such as solar radiation, temperature lapse rate, and wind characteristics are identified as causally associated with nitrogen dioxide concentrations, underscoring the complexity of pollutant dynamics. The exploration of nonlinear relationships between air pollutants and traffic factors using Generalized Additive Models (GAM) reveals optimal air quality scenarios contingent upon specific traffic conditions. Moreover, machine learning simulations indicate potential rises in pollutant levels under temperature increase scenarios, emphasizing the importance of proactive measures to address climate change and its impacts on air quality [18–22].

Other studies have explored the relationship between meteorological conditions and pollutants by examining the influence of meteorological factors on extreme levels of pollutants like $\text{PM}_{2.5}$ and O_3 or by investigating the spatiotemporal distribution of ground-level pollutants and their precursors. Some researchers have attempted to integrate air pollution waves, including $\text{PM}_{2.5}$, with cold waves to analyze temporal trends and spatial distributions of concurrent events. Additionally,

scientists have studied variations in $PM_{2.5}$ and O_3 , identifying points of change and quantifying the oscillatory relationships with meteorological factors across different time scales. These investigations employ various methods, including quantile regression, conventional analysis, generalized linear mixed models, Bayesian estimation, and wavelet coherence techniques. The findings underscore the complex dynamics between meteorological variables and extreme air pollution episodes, revealing varying sensitivities across different pollutants and regions. Surface winds and humidity emerge as significant drivers for high $PM_{2.5}$ events throughout the year, while summer O_3 extremes are predominantly by surface temperature. The high-performance Convolutional Neural Network (CNN) model unveils the nuanced interactions between factors influencing O_3 concentration, including wind direction, wind speed, temperature, and NO_2 concentration. Socioeconomic factors are crucial for predicting joint events, alongside meteorological and pollution factors, highlighting the need for holistic approaches in air quality management. Visibility, wind speed, precipitation, and cloud condition emerge as influential factors across all timescales and offer valuable insights for urban planning and air quality control strategies, particularly in cities affected by local climatic conditions. Additionally, the relationships between $PM_{2.5}$, O_3 and meteorological factors vary across different timescales, with combining multiple meteorological variables enhancing the understanding of variations, particularly on small scales. These comprehensive insights provide a basis for informed decision-making in mitigating air pollution and public health outcomes [23–27].

1.3. Motivation, Objectives, and research gap

Based on the research gap in most related work, this study is motivated by three key objectives:

- i. Identifying how atmospheric pollutants (O_3 , PM_{10} , NO_2 , SO_2 , and CO) relate to local meteorological factors (temperature, humidity, pressure, and wind speed) through multivariate analysis techniques, namely simple and multiple correlations, along with principal component analysis.
- ii. Based on our findings, we have identified the essential factors for improving predictions of O_3 and NO_2 pollution concentration using statistical and artificial intelligence models such as Multiple Linear Regression (MLR) and Two-layer Feed-forward Networks (TLFFN) supported by observation and reanalysis data. We have validated these results using data from three different periods in 2014, 2016, and 2018 for each pollutant (P1, P2, P3 for O_3 , and P1, P2, P4 for NO_2).
- iii. Building upon the results, we have used measurements from seven locations to forecast O_3 and NO_2 levels in sixteen districts using MLR and TLFFN models. We've employed a Quantum Geographic Information System (QGIS) for efficient mapping. Spatial data are analyzed and interpolated

using inverse distance weighted interpolation, providing precise predictions for the pollutants in the study area's districts.

This study presents a complete approach that can be adopted to generate pollution maps, especially in areas that suffer from a lack of stations. It can also be used to refine reanalysis data and reconstruct missing information. The rest of this article is structured as follows: Following the introduction, the Methodology section outlines our approach, covering the study area, statistical methods, and models utilized. Next, the Results and Discussion section presents our findings, including a discussion on the performance of our proposed model validated with data from 2014, 2016, and 2018, as well as data from the Copernicus Atmosphere Monitoring Service (CAMS) and a comparison with other studies. Lastly, the Conclusion section offers a findings summary, Limitations, Recommendations, and further directions. Fig. 1 presents the research strategy adopted in this study.

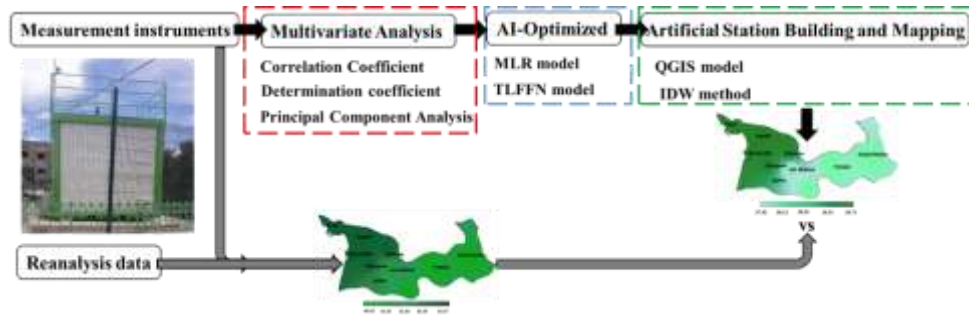


Fig. 1 – The research strategy adopted in this study

2. METHODOLOGY

2.1. Data Sets and Studied Area

Table 1 presents technical information on the dataset, variables, and study area. The city of Agadir currently hosts 5 air pollution monitoring stations, with 4 of them operational. For this study, observation data were collected from both mobile and fixed stations. The Ministry of the Interior is responsible for determining station locations and campaigns, while the General Directorate of Meteorology (DGM) oversees data collection and validation. The main data collected between February 1st and May 31st, 2016, while the validation data were obtained for four distinct periods: P1, P2, P3, and P4. Both stations facilitated the recording of hourly and daily averages for five pollutants (O_3 , PM_{10} , NO_2 , SO_2 , CO), alongside crucial local

meteorological parameters including temperature (T), relative humidity (RH), pressure (P), and wind speed (WS) [28]. We used data from the Copernicus Atmosphere Monitoring Service (CAMS) from the Centre for Medium-Range Weather Forecasts (ECMWF) to predict pollution in areas lacking measuring stations [29].

Fig. 2 shows the study area, including measurement and prediction sites. The present study was conducted in the prefectures of Agadir and Inezgane Ait Melloul, which together account for 42.42% of the population of the Souss Massa region, home to approximately 2.7 million inhabitants [30]. The measurement campaigns undertaken for this study covered various sites in the prefectures of Agadir. The climate of the studied area is influenced by three main factors: relief, the oceanic coast, and the Sahara Desert. In the northern part, dominated by the Atlas Mountains, the climate ranges from humid to semi-arid as it extends towards the plains. The plains, situated at the foothills of the Atlas Mountains and in the basins of the Souss and Massa rivers, experience an arid climate despite their proximity to the Atlantic Ocean. Lastly, the southern and southeastern parts of the region, bordering the Sahara Desert, exhibit a desert climate [31,32].

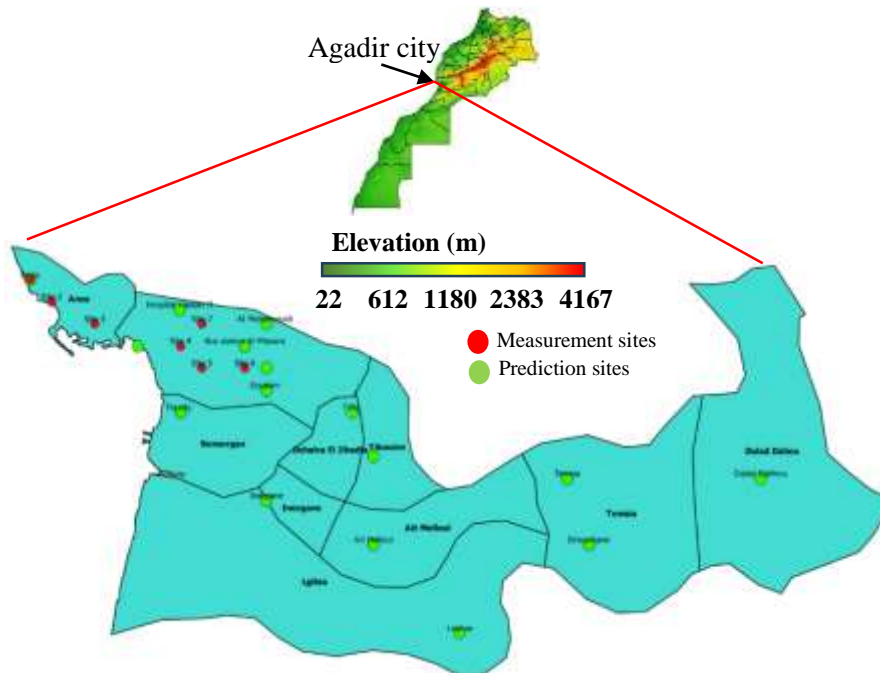


Fig. 2 – Study area mapping includes the Moroccan territory and the prefectures of Agadir and Inezgane-Ait Melloul

Table 1
Technical details: dataset, variables, and study area

Main data	<ul style="list-style-type: none"> • February 1st and May 31st, 2016
Validation data	<ul style="list-style-type: none"> • P1: 27-29 March 2014 • P2: 01-03 July 2016 • P3: 07-09 July 2018 • P4: 26-28 January 2018
Studied variables	<ul style="list-style-type: none"> • Pollutants: O₃, PM₁₀, NO₂, SO₂, and CO • Meteorological: T, RH, P, and WS
Predicted variables	<ul style="list-style-type: none"> • Pollutants: O₃, and NO₂
Studied Area	<ul style="list-style-type: none"> • Agadir and Inzegane-Ait Melloul prefectures

2.2. Multivariate methods

2.2.1. Simple and Multiple correlation

The first step in establishing the relationship between meteorological factors and pollutants is to compute the simple correlation coefficient. This coefficient, ranging from -1 to +1, quantifies the extent of the relationship between two variables. The use of a simple correlation enables the individual assessment of each meteorological parameter's impact on each pollutant. The Pearson correlation coefficient is then calculated by dividing the covariance of the two variables by the product of their standard deviations [33]. Given that cov represents the covariance, σ_X is the standard deviation of X , and σ_Y is the standard deviation of Y , the Pearson Correlation Coefficient (CC) is calculated using Eq. 1 [34]. The second step involves multiple correlation, conducted to ascertain the combined impact of various weather factors on each pollutant. Multiple correlation, represented by a value between 0 and +1, is determined using the coefficient of determination, which measures the degree of prediction for a given variable using a linear function of a set of other variables. It reflects the correlation between variables and the optimal linear predictions that can be derived from the predictive variables. The coefficient of determination (R^2) can be calculated by utilizing the vector of correlations between the predictor variables (independent variables) and the target variable, along with the correlation matrix displaying correlations among the predictor variables. Given that the predictor variables x_n , the target variable is y , C represents the vector of correlations, and R_{xx} is the correlation matrix. The coefficient of determination is determined using Eq. 2 [35].

$$cc = \frac{\text{cov}(x, y)}{\sigma_x \sigma_y} \quad (1)$$

$$R^2 = C^T R_{xx} C \quad (2)$$

2.2.2. Principal Component Analysis

To extract more information from the data and expressing this information as a set of summary indices called principal components (PCs). PC is used as a statistical technique to reduce the dimensions of a multivariate data set [36]. By implementing Principal Component Analysis (PCA), the Redundant information is removed, allowing this variable to be expressed in a smaller number of new variables as a linear combination of the original data with the same variance [37]. The linear combinations are named principal components or eigenvectors. The coefficient or load values in PCs are generated to indicating the origin variables relationships, saving the maximum variance as possible. PC1 collects the original data maximum variance and is associated with the highest eigenvalue. PC2 is orthogonal to PC1 and captures the variance not accounted for in the first PC. Generally, each successive PC maximizes the data variance not contained in the previous PCs. Also, the eigenvalue for each PC becomes smaller with each successive new PC. The highest eigenvalue indicates the maximum variance in the data, which helps identifying the number of PCs retained for interpretation. Let's assume we have a data matrix D with dimensions $n \times p$ where n is the number of observations and p is the number of variables. These steps in Table 2 provide a reduced representation of the original data in terms of principal components, capturing the essential variability in the original data.

Table 2

Key Steps of Principal Component Analysis

Steps	Definitions	Equations	
(1): Data Centering	Calculate the mean (\bar{D}) for each variable and subtract this mean from each element in the matrix D . This creates a new centered matrix, denoted as L .	$L = D - \bar{D}$	(3)
(2): Covariance Matrix	Compute the covariance matrix (C_{ov}) for the centered matrix L .	$C_{ov} = \frac{1}{n} L^T L$	(4)
(3): Eigenvectors and Eigenvalues	Compute the eigenvectors (v_i) and eigenvalues (λ_i) of the covariance matrix C_{ov} . These eigenvectors represent the principal components	$C_{ov} v_i = C_{ov} \lambda_i$	(5)
(4): Principal Components	Order the principal components based on the magnitude of their eigenvalues. The first few principal components explain the most significant variability in the data		

(5): Data Projection	Project the centered data L onto the selected principal components to obtain new coordinates. (where Y is the matrix of principal components, and V is the matrix of eigenvectors (principal components))	$Y = LV$	(6)
-------------------------	---	----------	-----

2.2.3. Statistical and neural network model

Multiple linear regression model, is a statistical technique used to predict the outcome of a response variable by utilizing several explanatory variables [38]. This model examines the relationship between multiple independent variables and a single dependent variable, assuming a linear connection between these variables. The general equation of a multiple linear regression model with n independent variables is expressed in Eq.7 [39]. Where Y is the dependent variable. β_0 is the intercept (the value of Y when all X variables are zero). β_n are the coefficients representing the change in Y for a one-unit change in each corresponding X variable while holding other variables constant. X_n are the independent variables. ε is the error term, representing unobserved factors affecting Y that are not accounted for in the model. The relationship between the variables is assumed to be linear, and the goal is to estimate the coefficients (β values) that best fit the observed data. This is typically done by minimizing the sum of squared differences between the observed and predicted values.

$$Y = \beta_0 + \beta_1 X_1 + \beta_2 X_2 + \dots + \beta_n X_n + \varepsilon \quad (7)$$

A two-layer feed-forward network with sigmoidal hidden neurons and linear output neurons can accurately adapt to multidimensional mapping problems [40]. A two-layer feed-forward neural network consists of an input set, a hidden layer, and an output layer. The input contains the features of the input data, the hidden layer performs transformations, and the output layer produces the final result. The model was configured with 10 hidden neurons, a single output layer, and the Levenberg-Marquardt backpropagation training algorithm was selected [41]. Data division was carried out by allocating 70% for training, 15% for validation, and 15% for testing, as shown in Table 1, using a sample division mode [42]. The performance function chosen to evaluate the model is the mean squared error (MSE). Additionally, data preparation involved the use of the mapminmax preprocessing function [43]. These configuration parameters determine how the artificial neural network will be trained and evaluated to solve our case study. Following our internal validation process, we employ distinct validation data (P1, P2, P3, and P4) that the model has not been exposed to, ensuring impartial assessment against observed values. Table 3 presents the operating steps of the TLFFN model.

Table 3
Operational Steps of the TLFFN Model

Steps	Definitions	Equations
(1): Initialization	Initialize the weights (W) and biases (b) of the neural network. This is typically done randomly.	$W_{ij}^{(1)}$ and $b_j^{(1)}$: hidden layer $W_{jk}^{(2)}$ and $b_k^{(2)}$: output layer (8)
(2): Forward Propagation	Compute the activations of the hidden layer and the output layer using the input data and the initialized weights and biases. σ represents an activation function	Hidden Layer Activation: $A_j^{(1)} = \sigma\left(\sum_{i=1}^N W_{ij}^{(1)} \cdot X_i + b_i\right)$ (9)
		Output Layer Activation: $A_k^{(2)} = \sum_{j=1}^M W_{jk}^{(2)} \cdot A_j^{(1)} + b_k^{(2)}$ (10)
(3): Loss Calculation	Compute the loss, which measures the difference between the predicted output and the true output (Y_i).	Mean Squared Error (MSE): $MSE = \frac{1}{2n} \sum_{i=1}^n (A_k^{(2)} - Y_i)^2$ (11)
(4): Backward Propagation	Compute the gradients of the loss with respect to the weights and biases, and update the weights and biases using an optimization algorithm. Weight and Bias Updates: $W_{ij}^{(1)}$ and $b_j^{(1)}$ are updated based on $\delta_j^{(1)}$ $W_{jk}^{(2)}$ and $b_k^{(2)}$ are updated based δ_k	Output Layer Error: $\delta_k = A_k^{(2)} - Y_i$ (12)
		Hidden Layer Error: $\delta_j^{(1)} = \sigma'(A_j^{(1)}) \left(\sum_{k=1}^M W_{jk}^{(2)} \cdot \delta_k\right)$ (13)
(5): Repeat	Repeat Steps 2-4 for a specified number of iterations (epochs) or until the loss converges to a satisfactory level.	
(6): Model Evaluation	Evaluate the trained model on a validation set or unseen data to assess its generalization performance.	

2.2.4. Inverse Weighting Distance in QGIS

Quantum Geographic Information System, developed in C++ and Python, stands as a leading free Geographic Information System for comprehensive geospatial tasks encompassing the creation, editing, visualization, analysis, and publication of geographic data. QGIS is an open-source design with a rich Python plugin development environment, making it the best choice for creating geoscience tools. Despite its versatility in handling various geographic data types, the Digital Elevation Models (DEMs) manipulation depicting global or local topography proves challenging, posing complexities in constructing paleo-geographic maps through its

underlying tools [44]. In this study, we have interpolated the predicted values of NO₂ and O₃ using Inverse Weighting Distance (IDW) method in QGIS. Considering some points i where the value of a given variable is measured and known, and one point j where the value is unknown, evaluate what the value at j may be from the values of the variable at points i , each measurement is assigned to the reference point after weighting by the inverse of the distance: the more distant monitoring stations are penalized. In what follows, the index i denotes a monitoring station, j is the index of a reference point and n_j is the number of monitoring stations that relate to the reference point j . Each measurement is multiplied by the inverse of distance $d_{ij} > 0$ from the station i to the reference point j with the exponent α , i.e., $\frac{1}{d_{ij}^\alpha}$. As this would change the magnitude of the final result, each product is divided by the sum of the terms $\frac{1}{d_{ij}^\alpha}$ over all stations. This amounts to defining the weights as indicated in Eq. 14. Therefore, pollution \bar{P}_j at the reference point j is given by Eq. 15, where P_{ij} is the pollution at the monitoring station i related to the reference point j . Combining Eq. 14 with Eq. 15 gives Eq. 16. Therefore, P_{ij} is weighted by the inverse of distance given the mean pollution \bar{P}_j at the reference point j , as presented in Eq. 17. For Air pollution, it was approved that IDW performs rather well when taking $\alpha = 2$, which justifies our choice for mapping NO₂ and O₃ predicted values over Agadir and Inzegane city.

$$W_{ij} = \frac{\frac{1}{d_{ij}^\alpha}}{\sum_{k=1}^{n_j} \frac{1}{d_{ik}^\alpha}} \text{ for any } i, j \quad (14)$$

$$\bar{P}_j = \sum_{i=1}^{n_j} W_{ij} P_{ij} \quad (15)$$

$$\bar{P}_j = \frac{\frac{1}{d_{ij}^\alpha}}{\sum_{k=1}^{n_j} \frac{1}{d_{ik}^\alpha}} P_{ij} \quad (16)$$

$$\sum_{i=1}^{n_j} W_{ij} = 1 \quad (17)$$

3. RESULTS AND DISCUSSION

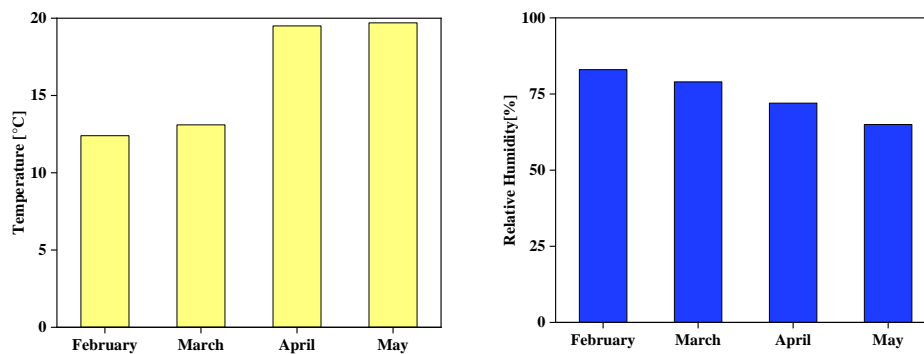
3.1. Meteorological and Trace Pollutant Analysis

Table 4 presents a statistical analysis of meteorological and trace pollutant. Additionally, Fig. 3 and 4 displays the monthly variation in these observed factors. Temperature averaged 16.2°C between a maximum of 28.1°C and a minimum of 9.2°C recorded on April 28th and February 06th, respectively. The standard deviation of this parameter shows a variability of around 3.9°C. The central temperature value is 17.4°C according to the median. The three potential extreme values are 12.6°C, 17.4°C and 19.3°C. Average relative humidity was 74%, ranging from a max of 93.7% on March 07th to a min of 36.4% on March 30th. The variability is 11.8%, with a central value of 75.4%. The RH data distribution presented three quartiles of 68.4%, 75.4%, and 84.2%. The pressure variation between 995.3 hPa and 1027 hPa observed justifies the variability of 10 hPa, presented by standard deviation. The median reflects the central value of 1006.8 hPa of the three potential pressure values of 1002.4 hPa, 1006.8 hPa, and 1020.0 hPa given by quartiles. Wind speeds ranged from 0.5 m/s to 2.8 m/s, observed on February 19th and May 13th. Processing the data in ascending order reveals a central value of 1.2 m/s, justified by the median. The three potential wind speed values according to quartiles are 0.9 m/s, 1.2 m/s, and 1.5 m/s, with a low variability of 0.4 m/s explained by the standard deviation. The interpretation of these results indicates a transition from late winter to early spring in February and March, followed by a shift to late spring or early summer conditions in April and May, characterized by warmer temperatures, decreasing humidity, and varying atmospheric pressure and wind speeds [45].

Average ozone concentrations reached 42.1 $\mu\text{g}/\text{m}^3$, ranging from a maximum of 65 $\mu\text{g}/\text{m}^3$ on May 04th to a minimum of 14.2 $\mu\text{g}/\text{m}^3$ on February 04th. Data variability was 10.2 $\mu\text{g}/\text{m}^3$, with a central value of 43.6 $\mu\text{g}/\text{m}^3$. The ozone data distribution shows three quartiles of 35.6 $\mu\text{g}/\text{m}^3$, 43.6 $\mu\text{g}/\text{m}^3$, and 50 $\mu\text{g}/\text{m}^3$. Ozone tends to increase between February and May, attributed to the sunshine increase from an average of 8 hours in February to an average of 11 hours in May. O_3 max does not exceed National standards requiring that 8-hour ozone concentrations remain below 110 $\mu\text{g}/\text{m}^3$. PM_{10} varied from 10.6 $\mu\text{g}/\text{m}^3$ to 179.6 $\mu\text{g}/\text{m}^3$, observed on February 06th and 19th, respectively. Order ascending treatment data reveals a central value of 55 $\mu\text{g}/\text{m}^3$, justified by the median. The three potential PM_{10} concentrations by quartile are 41.9 $\mu\text{g}/\text{m}^3$, 55.0 $\mu\text{g}/\text{m}^3$, and 73.7 $\mu\text{g}/\text{m}^3$, with a high variability of 29.4 $\mu\text{g}/\text{m}^3$ expressed by the standard deviation. It's important to highlight that the average PM_{10} concentration exceeds the limit recommended by the World Health Organization (WHO), which is 50 $\mu\text{g}/\text{m}^3$ averaged over 24 hours. This outcome is unsurprising given Agadir's status as a coastal city and a gateway to the Moroccan desert, facilitating the accumulation of aerosols, sea salt, and desert dust. Moreover, ongoing construction projects in the city contribute to this phenomenon.

The average NO_2 is $28.8 \mu\text{g}/\text{m}^3$, ranging from a maximum of $67.4 \mu\text{g}/\text{m}^3$ to a minimum of $16 \mu\text{g}/\text{m}^3$. The standard deviation of this parameter shows a variability around the mean of some $11.1 \mu\text{g}/\text{m}^3$. According to the median, the central NO_2 value is $24.1 \mu\text{g}/\text{m}^3$. The three potential extreme values are $21.0 \mu\text{g}/\text{m}^3$, $24.1 \mu\text{g}/\text{m}^3$, and $35.7 \mu\text{g}/\text{m}^3$. SO_2 ranges from $0 \mu\text{g}/\text{m}^3$ to $17 \mu\text{g}/\text{m}^3$ with an average value of $7.6 \mu\text{g}/\text{m}^3$. This pollutant has a variability of $4.8 \mu\text{g}/\text{m}^3$ with a central value of $8 \mu\text{g}/\text{m}^3$. The three potential concentrations of this pollutant are $3 \mu\text{g}/\text{m}^3$, $8 \mu\text{g}/\text{m}^3$ and $10 \mu\text{g}/\text{m}^3$. NO_2 and SO_2 pollutant levels are very far below the WHO limit of $200 \mu\text{g}/\text{m}^3$ over 1 hour and $20 \mu\text{g}/\text{m}^3$ averaged over 24 hours, respectively. CO presents a mean concentration of $60.2 \mu\text{g}/\text{m}^3$ between a maximum of $280 \mu\text{g}/\text{m}^3$ and a minimum of $10 \mu\text{g}/\text{m}^3$. This pollutant presents a large variability of $49.6 \mu\text{g}/\text{m}^3$, confirmed by the standard deviation and a central concentration of $\mu\text{g}/\text{m}^3$ valid by the median. The three potential concentrations of this pollutant are $30 \mu\text{g}/\text{m}^3$, $40 \mu\text{g}/\text{m}^3$, and $70 \mu\text{g}/\text{m}^3$. CO remains very low compared with the WHO standard alert of $10 \text{mg}/\text{m}^3$ as a maximum 8-hour daily average.

This pollution profile has already been observed in previous studies [46,47]. From Fig. 2 and 3, we can visualize profiles showing similar tendencies between the pollutants and meteorological parameters, such as ozone and temperature, or wind speed. To fully understand the nature of the relationship between meteorological parameters and pollution, we aim in the next section to identify the dependencies between atmospheric and meteorological pollutants using simple and multiple correlation and principal component analysis.



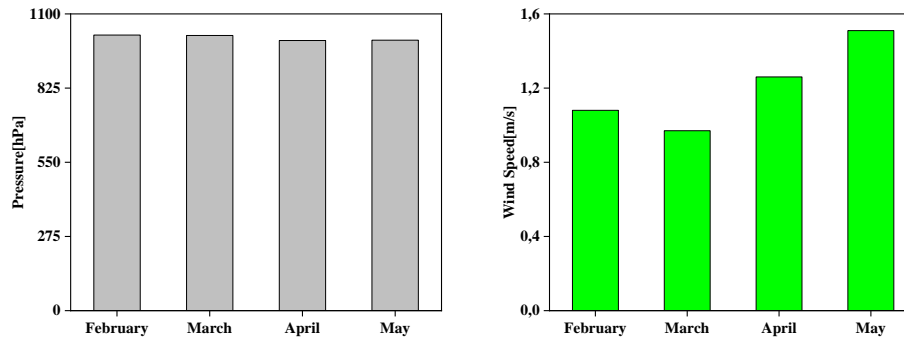
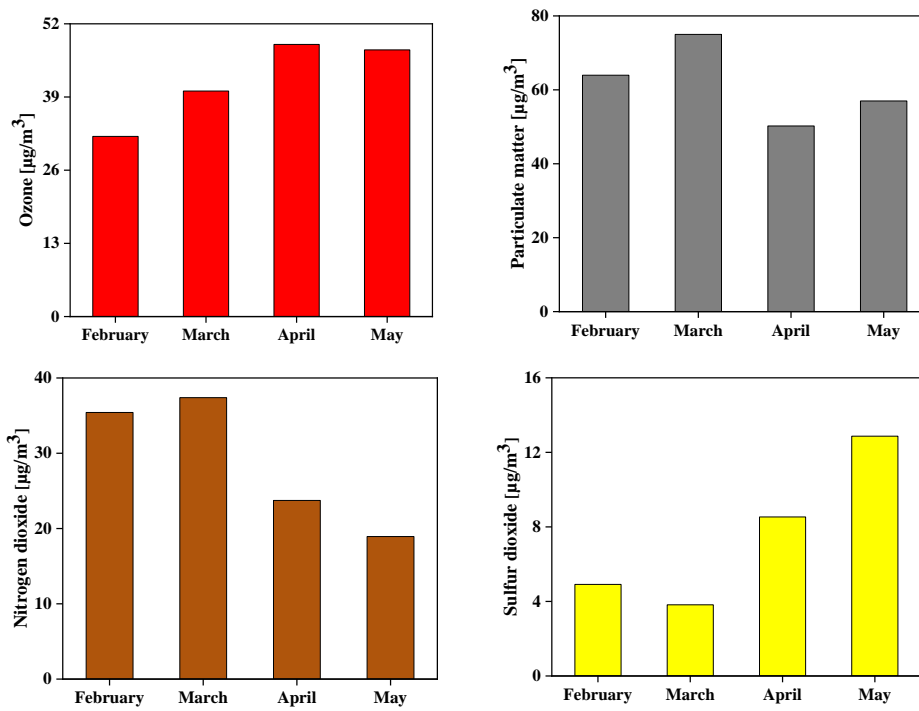


Fig. 3 – Monthly average of meteorological variables



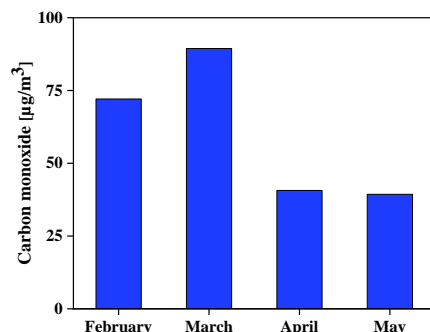


Fig. 4 – Monthly Average of Trace Pollutant

Table 4

Statistical Summary of Meteorological and Pollutant Data

	Mean	Max	Min	SD	Median	Quartiles		
						Q1	Q2	Q3
T[°C]	16.2	28.1	9.2	3.9	17.4	12.6	17.4	19.3
RH[%]	74.6%	93.7%	36.4%	11.8%	75.4%	68.4%	75.4%	84.2%
P[hPa]	1011.3	1027	995.3	10	1006.8	1002.4	1006.8	1020.0
WS[m/s]	1.2	2.8	0.5	0.4	1.2	0.9	1.2	1.5
O ₃ [µg/m ³]	42.1	65.0	14.2	10.2	43.6	35.6	43.6	50.0
PM ₁₀ [µg/m ³]	61.5	179.6	10.6	29.4	55.0	41.9	55.0	73.7
NO ₂ [µg/m ³]	28.8	67.4	16.0	11.1	24.1	21.0	24.1	35.7
SO ₂ [µg/m ³]	7.6	17	0.0	4.8	8.0	3.0	8.0	10.0
CO[µg/m ³]	60.2	280.0	10.0	49.6	40.0	30.0	40.0	70.0

3.2. Identification of meteorological Effects on Trace Pollutants

3.2.1. Simple and Multiple correlation

Fig. 5 (a) provides a simple correlation between pollutants and meteorological parameters. Substantial positive or negative correlations should align with underlying physical response mechanisms. Ozone concentration is moderately positively related to temperature and wind speed but negatively linked to relative humidity and strongly negatively correlated to atmospheric pressure. Temperature plays a crucial role in ozone formation, as higher temperatures can accelerate the photochemical reactions responsible for its production. Additionally, increased wind speed can also enhance the transport of ozone from distant sources into a region, potentially increasing local concentrations. Conversely, lower atmospheric pressure

conditions tend to hinder atmospheric mixing and reduce the dispersion of pollutants, including ozone [48,49].

The correlation of PM₁₀ with wind speed (-51%) indicates a strong negative relationship, suggesting that higher wind speeds effectively disperse PM₁₀ pollutants in the atmosphere, while lower wind speeds tend to result in their accumulation [50,51]. At higher temperatures, certain chemical reactions involving nitrogen oxides (NO_x), including NO₂, may accelerate to forming other pollutants such as O₃. Concurrently, increased wind speed promotes the movement and mixing of air masses, facilitating the dispersion of NO₂ throughout the atmosphere and subsequently reducing its local concentrations. However, the influence of high-pressure systems can offset this dispersion. High-pressure systems typically entail stable atmospheric conditions, which encourage the accumulation of NO₂ near the surface [52]. Temperature plays a crucial role in the behavior of sulfur dioxide (SO₂) in the atmosphere. For SO₂, temperatures may result in less vigorous vertical mixing of air masses, which can result in its buildup. Moreover, Relative humidity can influence the rates of chemical reactions involving sulfur dioxide. For example, humid conditions can enhance the oxidation of SO₂ to form CaCO₃ particles. The increase in atmospheric pressure favors the decrease in SO₂ concentrations. Additionally, atmospheric pressure changes can further influence SO₂ concentrations; an increase in pressure tends to favor the decrease in SO₂ concentrations [53]. Higher atmospheric pressure is often linked with elevated concentrations of carbon monoxide (CO) in the atmosphere. Conversely, higher wind speeds tend to be moderately correlated with lower CO concentrations, mainly attributed to the dispersion of CO [54].

To quantify the degree to which variations in pollutant levels can be attributed to changes in meteorological conditions, we studied the coefficient of determination between pollutants and combinations of meteorological parameters, namely T-RH, T-RH-P, and T-RH-P-WS, as shown in Fig. 5 (b). The T-RH combination explained 40.0% of ozone variability, while adding pressure increases ozone variation up to 60.0%, and with the contribution of wind speed, it reaches 64%. It suggests that increased temperature and wind speed, along with low humidity and pressure, favor the formation of tropospheric ozone, accounting for 64% of its variability. Such environmental conditions create a conducive atmosphere for the continued presence and accumulation of tropospheric ozone [55,56]. The T-RH combination accounts for only 11% of PM₁₀ variation. Adding pressure to the model increases this proportion to 38%, and with the inclusion of wind speed, it reaches 58%. This indicates that pressure plays a substantial role in influencing PM₁₀ levels beyond what temperature and relative humidity alone can explain. Finally, with the inclusion of wind speed, the ability to take PM₁₀ variation into account improves still further, reaching 58% [57]. The T-RH combination, indicating an ability to explain 53% of the nitrogen dioxide variation. The contribution of pressure increases considerably,

to 67%, and with the inclusion of wind speed, to 81%. This indicates that pressure significantly influences NO_2 levels beyond what temperature and relative humidity alone can explain. Moreover, incorporating wind speed into the model further enhances its capability to capture NO_2 variation, resulting in an improved explanatory power of 81% [58]. The T-RH combination explains 65% of the variation in sulfur dioxide. The addition of pressure does not increase this explained variation, maintaining it at 65% even with wind speed included. This implies that pressure does not notably add to the explanation of the variability in sulfur dioxide levels beyond what temperature and relative humidity already contribute. Sulfur dioxide, a prominent air pollutant, is frequently impacted by various emission sources [59]. Temperature and humidity combined account for 32% of carbon monoxide variability. By including pressure, this explained variation rises to 46%, and with the addition of wind speed, it reaches 53%.

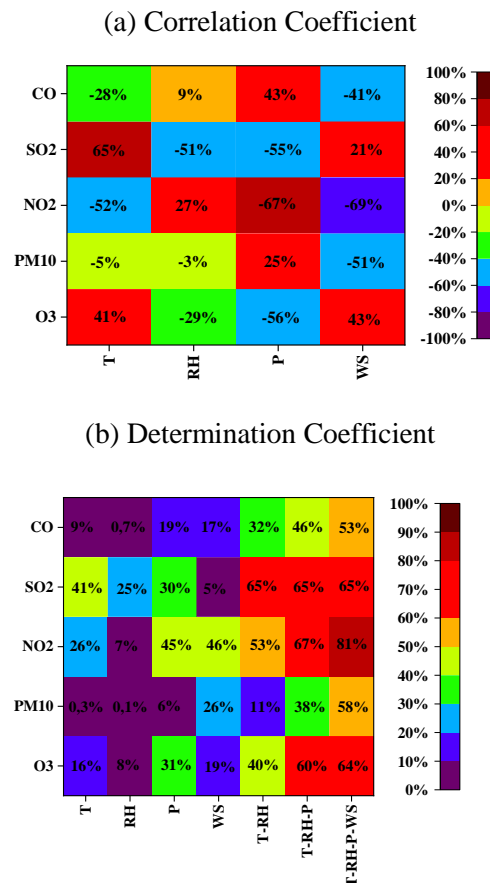


Fig. 5 – Correlation and Deterministic Coefficient between trace pollutants and meteorological parameters

3.2.2. Principal component Analysis

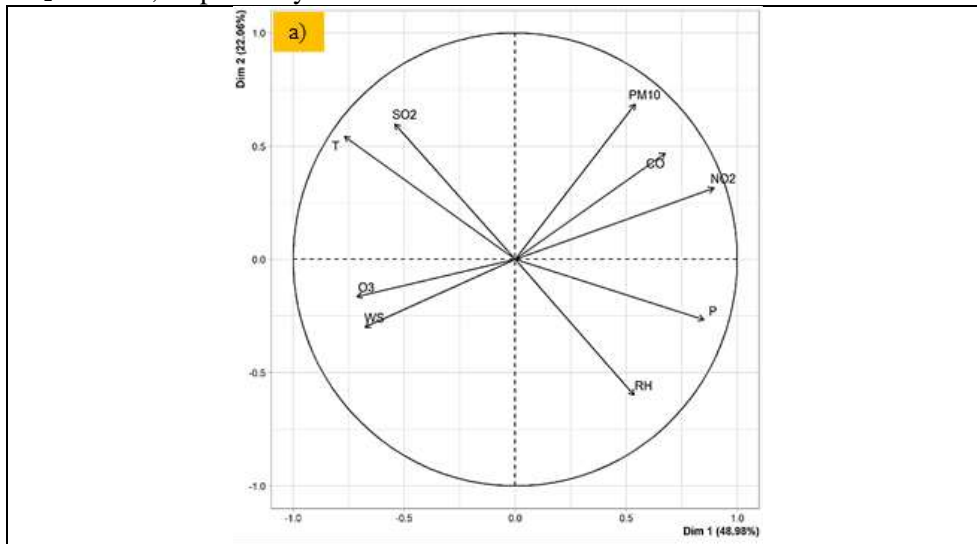
In the last section, we visualize simple and multiple correlations by analyzing the Pearson correlation and determination coefficient. In this section, we aim to reduce the dimensionality of the data and preserve as much of their information structure as possible. Of the nine principal components presented by the PCA method illustrated in Table 5, the first two (PC1 and PC2) have eigenvalues greater than 1 (Kaiser criterion) and account for 71.04% of the observed variation in the data, enabling them to be used for subsequent interpretation. Table 5 summarizes the load values of the first two principal components (PC1 and PC2) for meteorological parameters and pollutants. Only absolute load values greater than or equal to 0.3 (values in bold) contribute to PC interpretations. PC1 is significantly influenced by atmospheric pressure, Nitrogen dioxide, Carbon monoxide, wind speed, and PM₁₀ particles. It is negatively affected by temperature, Ozone, Sulfur dioxide, and wind speed. PC2 is principally affected by Temperature, PM₁₀, SO₂, and CO particles, which vary positively in this dimension. Relative humidity has a negative influence.

According to these results, the decrease in O₃ and SO₂ concentrations is favored by meteorological conditions characterized by an increase in pressure and relative humidity, and a decrease in temperature and wind speed, and vice versa. This observation is further supported by Fig. 5(a). Additionally, SO₂ demonstrates a second trend, associating the increase in this pollutant with rising temperatures and decreasing humidity. PM₁₀, NO₂, and CO exhibit two profiles: the first aligns with PC1, and the second aligns with PC2. These two profiles suggest that the increase in PM₁₀, NO₂, and CO is influenced by two distinct sets of climatic conditions. The first set is characterized by an increase in humidity and pressure, coupled with a decrease in temperature and wind speed. Conversely, the second set is marked by a rise in temperature and lower humidity.

Fig. 6 (a) shows the plot of meteorological variables and pollutants for PC1 and PC2. This figure justifies explicitly the results in Table 4 and allows us to group these studied variables into four groups. The 1st is composed of PM₁₀, CO, and NO₂, which may mean that these pollutants react positively to the same factors, such as similar emissions, specific meteorological conditions, or indirect chemical reactions [60]. For example, the indirect chemical reactions that can link CO and NO₂ are shown in Eq 18, where OH represents the hydroxy radical, HO₂ represents the hydroperoxyl radical, and NO₃ represents nitrogen trioxide. It became apparent that notable correlations existed between PM₁₀ and SO₂, attributable to the presence of H₂SO₄ as fine atmospheric particles, where SO₂ plays a pivotal role as a primary precursor in its generation [61], as indicated in Eq 19. M represents a third body, typically a collision partner like a nitrogen molecule (N₂) or oxygen molecule (O₂)

that helps in the energy transfer during the reaction. The 2nd is SO₂ and T, suggesting that variations in temperature could lead to reduced intensity in the vertical mixing of air masses [62]. The 3rd is RH and P, indicating perhaps the same effect of both parameters on pollutants like O₃ and NO₂ in our case (Fig. 5). The 4th is O₃ and WS, implying higher wind speed levels are associated with higher ozone concentrations [63].

Fig. 6 (b) plots the individuals of PC2 versus PC1. The individual data in the red rectangle are identified by a significant temperature contribution, with an average of 20.42°C and high SO₂ concentrations averaging 12.53µg/m³, derived from 8 days in April and 24 days in May. The individuals in the gray box are characterized by a significant effect of wind speed with an average of 1.62 m/s and O₃ concentration averaging 48 µg/m³, originating from 9 days of April. In the green rectangle, individual data are recognized by the high-pressure average of 1022.39 hPa and the high humidity average of 85%, obtained over 13 and 10 days in February and March, respectively. Refer to the extreme individuals in the blue circle, the three individuals 15,19, and 57, representing 15 and 19 February and 29 March, are characterized by maximum values for PM₁₀ (150.26 µg/m³ on average), CO (202.48 µg/m³ on average), and NO₂ (57.57 µg/m³ on average). The extremes 87 and 88 (29 and 30 April) are identified by maximum temperatures (average of 25°C) and SO₂ values (average of 12.5 µg/m³). Extreme 6, 7, 8, and 9, corresponding to 06, 07, 08, and 09 February, are characterized by the combinatorial effect of high humidity (89.97% on average) and wind speed (1.8 m/s on average), with moderate pollution of 37.39 µg/m³, 15.17 µg/m³, 19.64 µg/m³, 1.71 µg/m³ and 17.31 µg/m³ for O₃, PM₁₀, NO₂, SO₂ and CO, respectively.



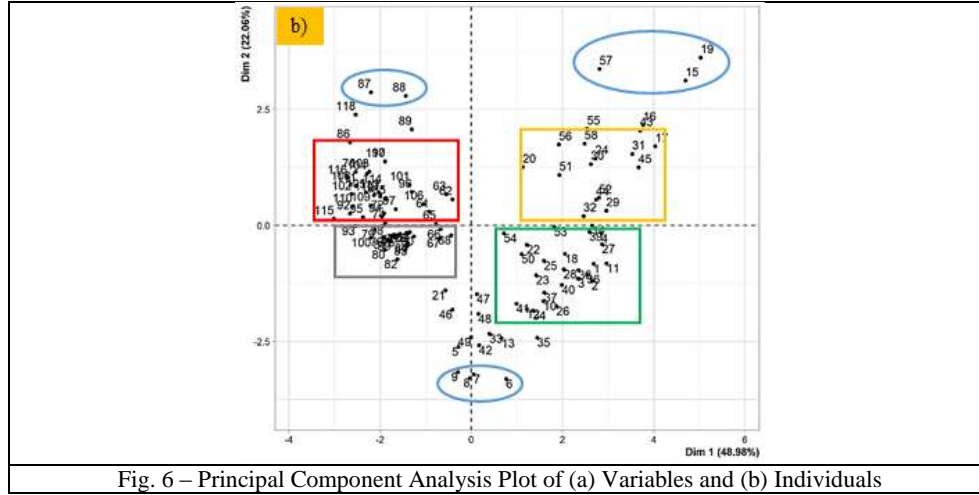
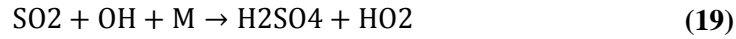
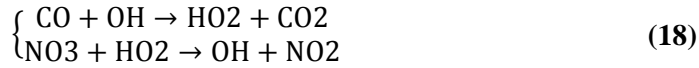


Fig. 6 – Principal Component Analysis Plot of (a) Variables and (b) Individuals



3.3. Optimized Trace Pollutants Forecasting

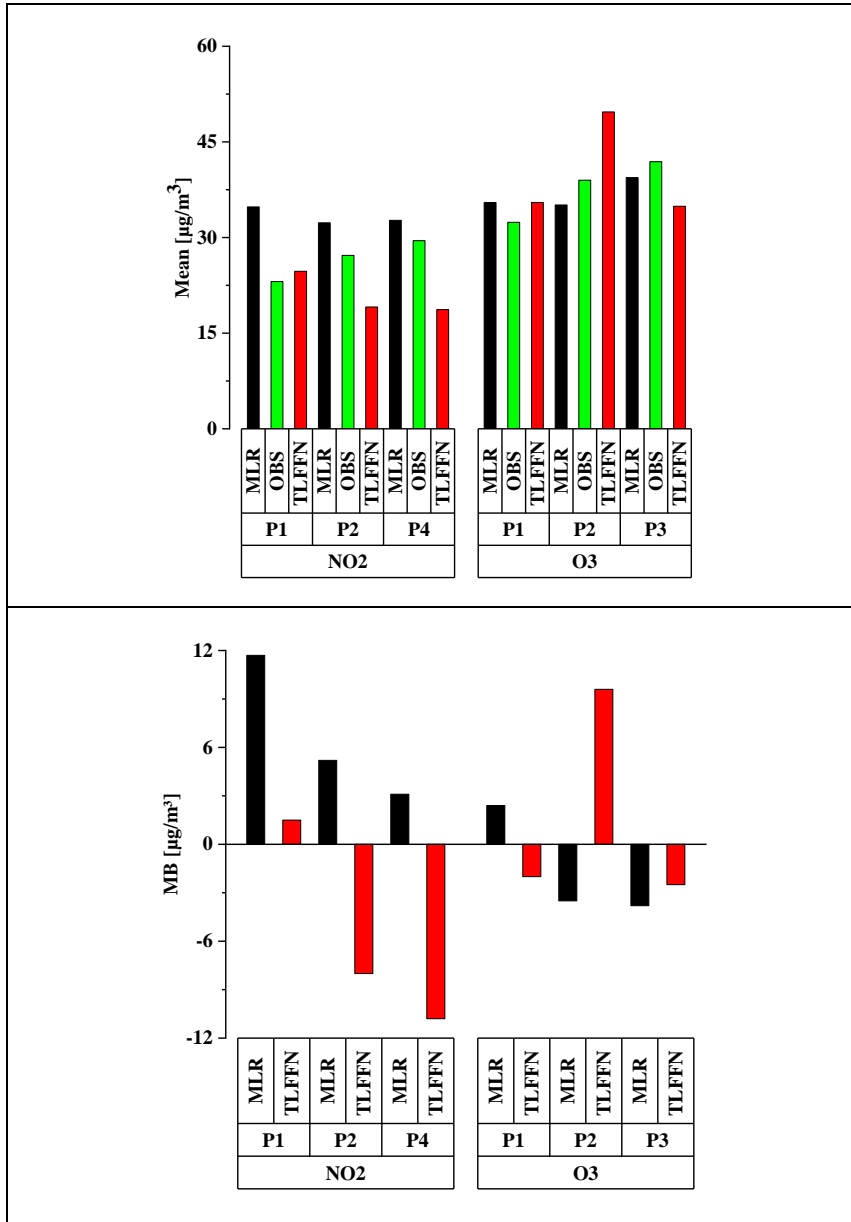
Based on the results of identifying the relationship between pollutants and meteorological parameters, we have selected two pollutants, O_3 and NO_2 , due to their variability in correlation with meteorological conditions and their representativeness (absolute eigenvalue > 0.7) concerning the two main components, PC1 and PC2. During the construction phase of the MLR and TLFFN models, the selection of inputs is guided by the relationships already identified between the chosen pollutants for predicting meteorological parameters and other pollutants. The inputs for O_3 include temperature, wind speed, ozone, and sulfur dioxide. NO_2 considers pressure, and CO as its inputs. Meteorological input data is acquired through observations at each site, while pollutant input data is obtained from the European Centre for Medium-Range Weather Forecasts. The validation of results for each pollutant is conducted separately for the three periods, as indicated in Fig. 7 (The formulas for Mean bias (MB) and Root means square error (RMSE) are mentioned in Table 5)

For ozone, the best correlations (96% and 97%) are obtained for P2, which is expected since the training, validation, and test data date from 2016. However, during this same period, there were high RMSEs of $10.2 \mu\text{g}/\text{m}^3$ and $5.5 \mu\text{g}/\text{m}^3$ for TLFFN and MLR, respectively. The explanation may lie in the contribution of local

emissions or in the seasonal variability that the two models are unable to capture, as indicated by P3. Despite this, both models show acceptable correlations with low RMSEs for P1 and P2, indicating that the models have effectively captured spatial variability, considering that the measurements take place in different areas during these two periods. These results are comparable to and outperform other studies [50,64]. Generally, for ozone, it is recommended to use the MLR model due to its ability to capture the trend (good correlation) and its accuracy (low RMSE). This suggests that the linear relationship between inputs and outputs is extensively sufficient to capture good ozone predictions, making it easy to interpret the impact of each predictor on the outcome [65]. However, it should be noted that other studies utilizing MLR have yielded moderate results, which may vary depending on factors such as the nature of the data, the time period considered, and the study methodology [66].

For nitrogen dioxide, variability in correlation and RMSE can be observed, which may be due to the fact that this pollutant is mostly related to emissions. The TLFFN model demonstrates strong stability in predicting NO₂, compared to the unstable MLR model. The low MLR correlation in P1 may be due to the high CO concentration observed in this period (CO(P1) = 53.6 µg/m³, CO(P2) = 39.9 µg/m³, and CO(P4) = 48.0 µg/m³). The MLR model tends towards overestimation, whereas TLFFN varies between overestimation and underestimation. These results are superior to those obtained in other studies using deterministic, statistical, or artificial intelligence models [67–69]. Therefore, the TLFFN model is recommended for predicting NO₂ concentrations, unlike ozone [70]. The prediction of NO₂ exhibits a non-linear relationship with the input variables (as revealed by Eq. 18), suggesting that neural networks, with their ability to capture intricate non-linear relationships between predictors and outputs, are better suited for this task [71].

The ability of this strategy, which is based on identifying relationships between atmospheric and meteorological pollutants to optimize and select input variables and predict O₃ and NO₂ emissions using both statistical and artificial intelligence methods, lies firstly in its capacity to capture both linear and non-linear relationships between inputs and outputs. Secondly, comparing each model with the other provides valuable insights into pollutant dispersion, particularly O₃ and NO₂, which exhibit an inverse relationship (as demonstrated by Eq. 20 and observed in Fig. 6(a)), especially in areas lacking measuring stations. This strategy can be employed to correct bias and trends, as well as predict missing data. Based on these performance results, the objective is to predict O₃ and NO₂ to map these pollutants over the Agadir and Inzegane-Ait Melloul prefectures.



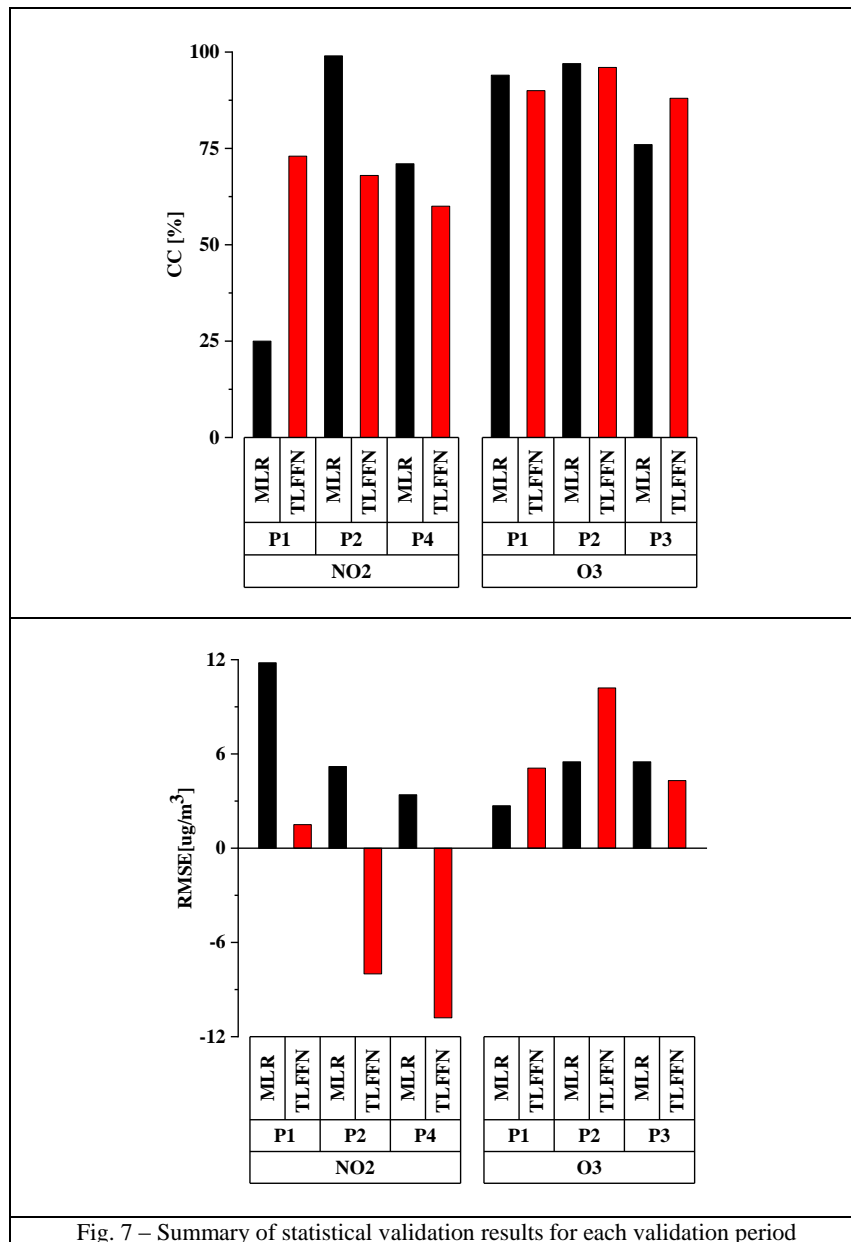


Table 5

Mean bias (MB) and Root means square error (RMSE)

$$\begin{aligned}
 \mathbf{MB} &= \frac{\sum_{k=1}^n (\mathbf{M}_k - \mathbf{O}_k)}{n} \\
 \mathbf{RMSE} &= \sqrt{\frac{\sum_{k=1}^n (\mathbf{M}_k - \mathbf{O}_k)^2}{n}} \quad [72]
 \end{aligned}$$

3.4. Mapping Optimized Trace Pollutants Forecasting

Fig. 8 and 9 compare ozone and nitrogen dioxide maps using MLR, TLFFN, and reanalysis for P1, P2, and P3. The mapping process encompasses the urban areas of two prefectures: Agadir, spanning 2297 km² and inhabited by 682 110 people, and Inzegane-Ait Melloul, covering 297 km² with a population of 628 390. It represents the first of its kind to be produced in this region. Measures are taken at seven sites to predict O₃ and NO₂ in sixteen districts (Fig.2) using the two methods adopted in this study, Multiple Linear Regression and Two-Layer Feedforward Neural Network. Fig. 1, Table 6 display the position and the coordinates of seven measurement sites and sixteen prediction districts, respectively. The mapping process utilizes a Quantum Geographic Information System to execute the task efficiently. Employing inverse distance weighted interpolation, spatial data is analyzed and interpolated, ensuring accurate predictions for the targeted pollutants across the study area's districts. The initial observation from Fig. 7 indicates that ozone concentrations are slightly higher in the Agadir prefecture compared to the Inzegane-Ait Melloul prefecture. This could be because there is a slight rise in the sale of electrical energy and petroleum product consumption in Agadir compared to Inzegane-Ait Melloul, as shown in Fig. 10 (b). The MLR model outperforms TLFFN, accurately reproducing the reanalysis maps for all three periods studied, with mean spatial bias ranging from 1.47 µg/m³ to 6.21 µg/m³, as shown in Fig. 10 (a). Given these positive outcomes, using the MLR model for prediction combined with QGIS and IDW for interpolation could be adopted to generate ozone maps [73,74], providing decision-makers with a comprehensive perspective on ozone dispersion.

The initial finding about NO₂ in Fig. 8 shows a low unusual concentration in the reanalysis data. Many studies are looking into this emissions problem in their models and trying to fix it. This problem mainly happens because of the short lifetime of NO₂ and the high variability of concentrations, making it hard to validate with observations [75]. Even though energy sales are similar, the Inzegane-Ait Melloul prefecture has slightly higher NO₂ compared to Agadir. This is because of the intense farming activity in this area, as indicated in Fig. 10 (b), supported by several studies confirming agriculture as a source of NO₂ [76]. Nevertheless, the

TLFFN model displays a comparable pattern to the reanalysis maps in contrast to MLR, indicating a tendency for TLFFN to underestimate and MLR to overestimate, as depicted in Fig. 7 and Fig. 10 (a). Using QGIS alongside IDW coupled with TLFFN could offer a method for refining NO₂ reanalysis data and reconstructing missing information [77], which would prove advantageous for various atmospheric pollution modeling endeavors across the study area.

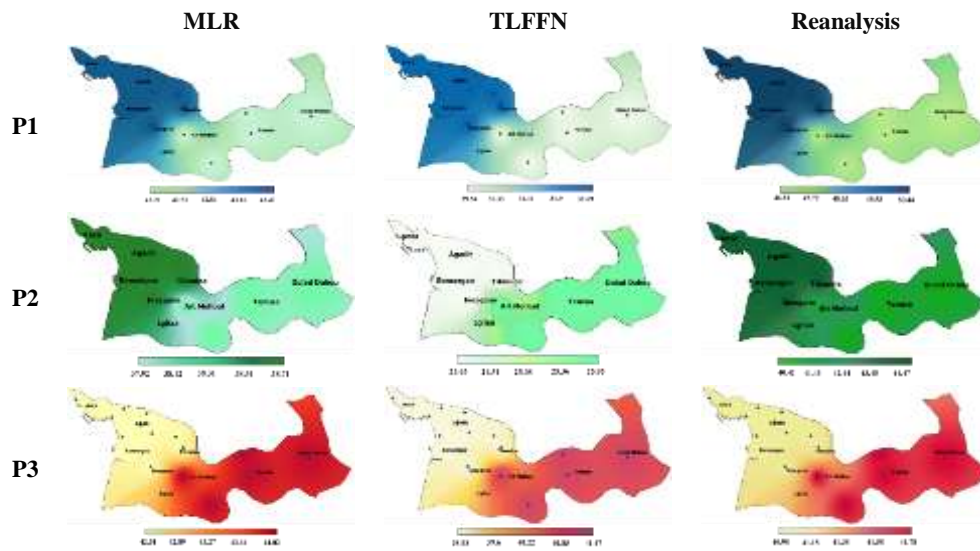


Fig. 8 – Comparison of ozone mapping over the studied area using MLR, TLFFN Models, and reanalysis data for each validation period over studied area

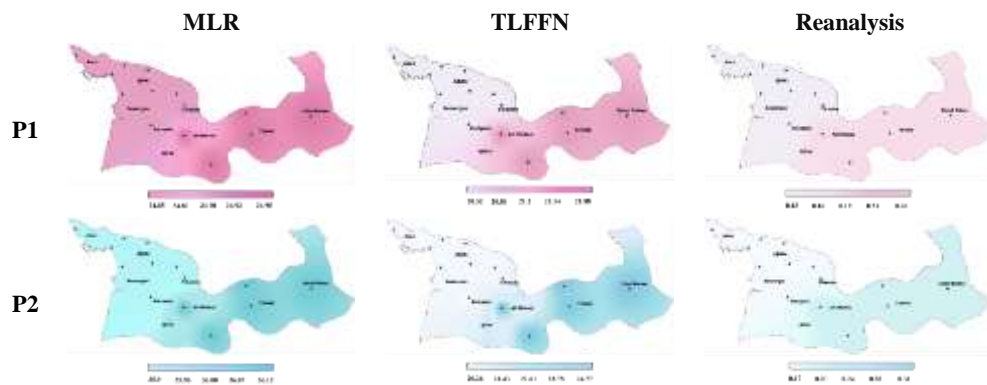




Fig. 9 – Comparison of nitrogen dioxide mapping over the studied area using MLR, TLFFN Models, and reanalysis data for each validation period

Table 6

Coordinates of seven measurement sites and sixteen prediction districts

	Prediction sites			Measurement sites		
		Lon[°]	Lat[°]		Lon[°]	Lat[°]
Agadir prefecture	District1	-9,65704	30,44605	Site 1	-9,66	30,45
	District2	-9,60801	30,42413	Site 2	-9,65	30,44
	District3	-9,59038	30,43637	Site 3	-9,63	30,43
	District4	-9,56574	30,41637	Site 4	-9,59	30,42
	District5	-9,55633	30,430099	Site 5	-9,58	30,41
	District6	-9,59238	30,39607	Site 6	-9,56	30,41
	District7	-9,54926	30,40067	Site 7	-9,58	30,43
	District8	-9,559	30,41565			
	District9	-9,51451	30,39608			
	District10	-9,50339	30,37976			
Inzegan- Ait Melloul prefecture	District11	-9,55149	30,35231			
	District12	-9,50402	30,33792			
	District13	-9,46448	30,29692			
	District14	-9,40755	30,33961			
	District15	-9,41449	30,36909			
	District16	-9,32084	30,36512			

a) Mean spatial bias

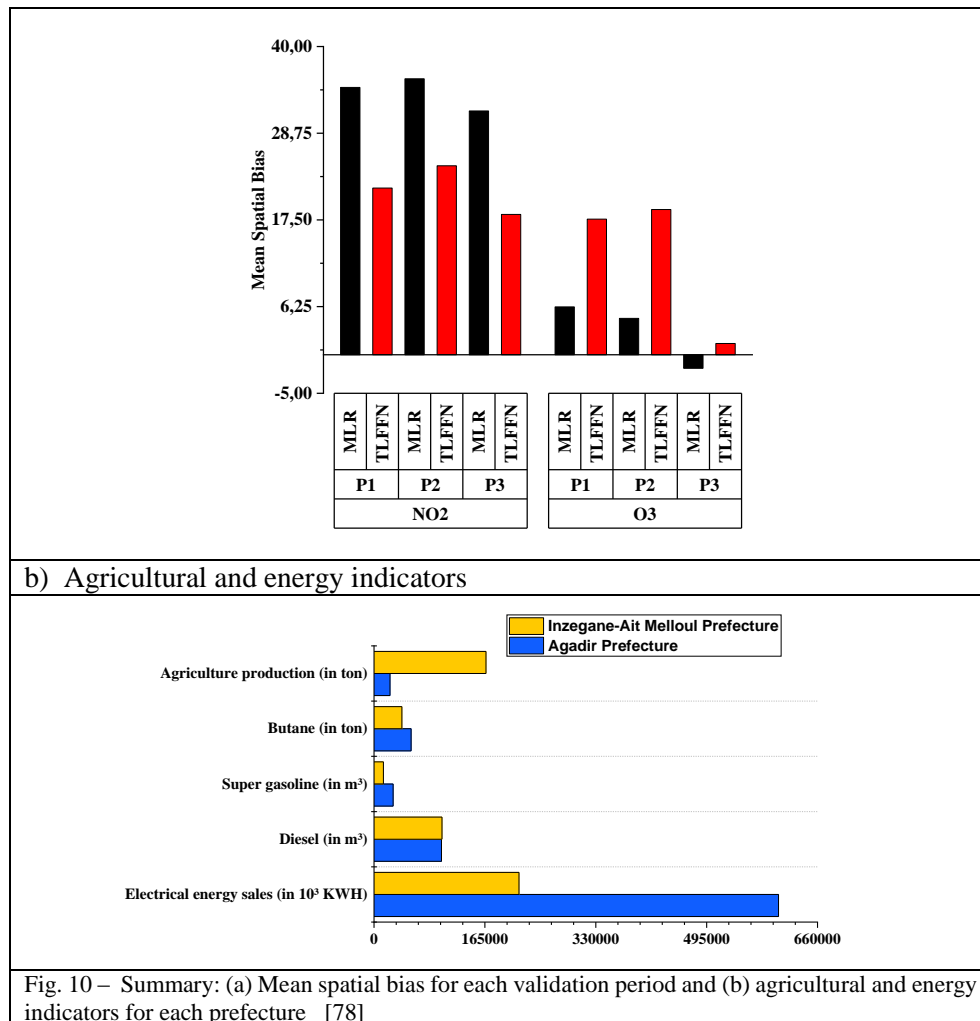


Fig. 10 – Summary: (a) Mean spatial bias for each validation period and (b) agricultural and energy indicators for each prefecture [78]

4. CONCLUSIONS AND RECOMMENDATIONS

This study thoroughly examined how air pollutants like O₃, NO₂, SO₂, and CO relate to local weather factors such as temperature, humidity, pressure, and wind speed. Advanced techniques are used to analyze these complex interactions, like simple and multiple correlations, along with principal component analysis. By doing so, we pinpointed crucial factors that can enhance predictions of O₃ and NO₂. We employed statistical methods like multiple linear regression and artificial intelligence models, such as two-layer feedforward networks. These models were

tested using observational from three periods (2014, 2016, and 2018). We used the findings and data from seven locations and reanalysis to forecast O₃ and NO₂ levels in sixteen districts. Using the Quantum Geographic Information System and employed inverse distance weighted interpolation for precise spatial analysis to visualize and map these forecasts effectively. The principal findings of the study are as follows :

- According to ACP findings, O₃ is influenced by temperature, wind speed, and sulfur dioxide, while NO₂ takes into account pressure and CO as its contributing factors.
- Using the MLR model for ozone prediction is recommended because of its ability to capture trends and maintain accuracy, indicating a sufficient linear relationship between inputs and outputs. This makes it easy to interpret the impact of each predictor on ozone outcomes.
- The TLFFN model is suggested for predicting NO₂ concentrations due to its capability to capture non-linear relationships between predictors and outputs. Unlike ozone, NO₂ predictions benefit from neural networks' ability to handle intricate non-linear relationships effectively.
- Using the MLR model for prediction alongside QGIS and IDW for interpolation can generate ozone maps, offering decision-makers a comprehensive view of ozone dispersion.
- Utilizing QGIS with IDW, combined with TLFNN, provides a method to refine NO₂ reanalysis data and reconstruct missing information, advantageous for atmospheric pollution modeling in the study area.

The proposed approach offers an initial opportunity to visualize air pollution in central Morocco, aiding municipal planning. Expanding and refining this approach could turn it into a national strategy, especially given Morocco's lack of national maps based on air pollution observations. To strengthen this approach, integrating satellite data can enhance the availability of variables challenging to measure directly. Additionally, deterministic models can provide insights, especially in remote or inaccessible areas where direct measurements are challenging.

ACKNOWLEDGMENTS

The Hungarian University of Agriculture and Life Sciences and University IBN Zohr, particularly the Faculty of Sciences, have assisted in this research at all stages. We warmly acknowledge the Department of Energy and Environment of the Souss-Massa region for their cooperation. We also appreciate the precious aid of the General Directorate of Meteorology (GDM).

REFERENCES

1. A. Huang, M. Chu, W. Cheng, G. Wang, P. Guan, L. Zhang, and J. Jia, *Dynamic evaluation of China's atmospheric environmental pressure from 2008 to 2017: Trends and drivers*, J. Environ. Sci. **150**, 177 (2025). <https://doi.org/https://doi.org/10.1016/j.jes.2024.02.017>.
2. A. Ajdour, B. Ydir, J. Chaoufi, R. Leghrib, *An advanced hybrid model based on stochastic - Eulerian numerical approach: Application to atmospheric pollution*, Rom. J. Phys. **69**, 808 (2024). <https://doi.org/10.59277/RomJPhys.2024.69.808>
3. A. Ajdour, A. Adnane, B. Ydir, D. Ben hmamou, K. Khomsi, H. Amghar, Y. Chelhaoui, J. Chaoufi, and R. Leghrib, *A new hybrid models based on the neural network and discrete wavelet transform to identify the CHIMERE model limitation*, Environ. Sci. Pollut. Res. **30**, 13141 (2023). <https://doi.org/10.1007/s11356-022-23084-8>.
4. M.-V. BIRSAN, I.-A. NITA, and V.-A. AMIHĂESEI, *INFLUENCE OF LARGE-SCALE ATMOSPHERIC CIRCULATION ON ROMANIAN SNOWPACK DURATION*, Rom. Reports Phys. **76**, 708 (2024). <https://doi.org/10.59277/RomRepPhys.2024.76.708>
5. A. Ajdour, B. Ydir, H. Bouzghiba, I. D. Sulaymon, A. Adnane, D. Ben Hmamou, K. Khomsi, J. Chaoufi, G. Géczy, and R. Leghrib, *Investigating Two-dimensional Horizontal Mesh Grid Effects on the Eulerian Atmospheric Transport Model Using Artificial Neural Network*, Aerosol Air Qual. Res. **24**, 230309 (2024). <https://doi.org/10.4209/aaqr.230309>.
6. B. P. Nandi, G. Singh, A. Jain, and D. K. Tayal, *Evolution of neural network to deep learning in prediction of air, water pollution and its Indian context*, Int. J. Environ. Sci. Technol. **21**, 1021 (2024). <https://doi.org/10.1007/s13762-023-04911-y>.
7. M. Imam, S. Adam, S. Dev, and N. Nesa, *Air quality monitoring using statistical learning models for sustainable environment*, Intell. Syst. with Appl. **22**, 200333 (2024). <https://doi.org/10.1016/j.iswa.2024.200333>.
8. A. Tateo, V. Campanaro, N. Amoroso, L. Bellantuono, A. Monaco, E. Pantaleo, R. Rinaldi, and T. Maggipinto, *Predicting Air Quality from Measured and Forecast Meteorological Data: A Case Study in Southern Italy*, Atmosphere. **14**, 475 (2023). <https://doi.org/10.3390/atmos14030475>.
9. A. Adnane, A. Ajdour, R. Leghrib, J. Chaoufi, and A. Chirmata, *A Comparative Study Between NARX and LSTM Models in Predicting Ozone Concentrations: Case of Agadir City (Morocco)*, AI IoT Sustain. Dev. Emerg. Countries, Challenges Oppor. **105** pp. 189–198 (2022). https://doi.org/10.1007/978-3-030-90618-4_9.
10. A. González-Vidal, A. Martínez-Ibarra, and A. F. Skarmeta, *MultiBEATS: Blocks of eigenvalues algorithm for multivariate time series dimensionality reduction*, Inf. Fusion **104**, 102159 (2024). <https://doi.org/10.1016/j.inffus.2023.102159>.
11. S. R. Shams, S. Kalantary, A. Jahani, S. M. Parsa Shams, B. Kalantari, D. Singh, M. Moeinnadini, and Y. Choi, *Assessing the effectiveness of artificial neural networks (ANN) and multiple linear regressions (MLR) in forecasting AQI and PM10 and evaluating health impacts through AirQ+ (case study: Tehran)*, Environ. Pollut. **338**, 122623 (2023). <https://doi.org/10.1016/j.envpol.2023.122623>.
12. A. Singh, M. Mehra, A. Kumar, M. Niranjannaik, D. Priya, and K. Gaurav, *Leveraging hybrid machine learning and data fusion for accurate mapping of malaria cases using meteorological variables in western India*, Intell. Syst. with Appl. **17**, 200164 (2023). <https://doi.org/10.1016/j.iswa.2022.200164>.
13. Y. Saliba and A. Bărbulescu, *A comparative evaluation of spatial interpolation techniques for maximum temperature series in the montreal region, canada*, Rom. Reports Phys. **76**, 701 (2024). <https://doi.org/10.59277/RomRepPhys.2024.76.701>.
14. U. Krishnamoorthy, V. Karthika, M. K. Mathumitha, H. Panchal, V. K. S. Jatti, and A. Kumar, *Learned prediction of cholesterol and glucose using ARIMA and LSTM models – A comparison*, Results Control Optim. **14**, 100362 (2024). <https://doi.org/10.1016/j.rico.2023.100362>.

15. S. K. Natarajan, P. Shanmurthy, D. Arockiam, B. Balusamy, and S. Selvarajan, *Optimized machine learning model for air quality index prediction in major cities in India*, *Sci. Rep.* **14**, 6795 (2024). <https://doi.org/10.1038/s41598-024-54807-1>.
16. T. Al Smadi, A. Handam, K. S. Gaeid, A. Al-Smadi, Y. Al-Husban, and A. smadi Khalid, *Artificial intelligent control of energy management PV system*, *Results Control Optim.* **14**, 100343 (2024). <https://doi.org/10.1016/j.rico.2023.100343>.
17. P. Aszkowski, B. Ptak, M. Kraft, D. Pieczyński, and P. Drapikowski, *Deepness: Deep neural remote sensing plugin for QGIS*, *SoftwareX* **23**, 101495 (2023). <https://doi.org/10.1016/j.softx.2023.101495>.
18. M. P. Liphonhay, A. V Valerio, and C. P. Monterola, *Time-delayed causal network analysis of meteorological variables and air pollutants in Baguio city*, *Atmos. Pollut. Res.* 102095 (2024). <https://doi.org/10.1016/j.apr.2024.102095>.
19. Yuval, Y. Levi, and D. M. Broday, *Revealing causality in the associations between meteorological variables and air pollutant concentrations*, *Environ. Pollut.* **345**, 123526 (2024). <https://doi.org/10.1016/j.envpol.2024.123526>.
20. Y. Han, W. Zhao, and P. Pereira, *Global COVID-19 pandemic trends and their relationship with meteorological variables, air pollutants and socioeconomic aspects*, *Environ. Res.* **204**, 112249 (2022). <https://doi.org/10.1016/j.envres.2021.112249>.
21. Y.-C. Lin, Y.-T. Lin, C.-R. Chen, C.-Y. Lai, and Y.-B. Wang, *Meteorological and traffic effects on air pollutants using Bayesian networks and deep learning*, *J. Environ. Sci.* 1 (2024). <https://doi.org/10.1016/j.jes.2024.01.057>.
22. A. N. Brum, R. de L. Brum, A. da S. Bonifácio, F. M. R. da Silva Júnior, and L. Zhang, *Impact of temperature increase on air pollutants - A case study in a small city in southern Brazil*, *Case Stud. Chem. Environ. Eng.* **9**, (2024). <https://doi.org/10.1016/j.cscee.2024.100624>.
23. X. Zhang, X. Xiao, F. Wang, G. Brasseur, S. Chen, J. Wang, and M. Gao, *Observed sensitivities of PM_{2.5} and O₃ extremes to meteorological conditions in China and implications for the future*, *Environ. Int.* **168**, 107428 (2022). <https://doi.org/10.1016/j.envint.2022.107428>.
24. Q. Wang, D. Sheng, C. Wu, X. Ou, S. Yao, J. Zhao, F. Li, W. Li, and J. Chen, *Investigation of spatiotemporal distribution and formation mechanisms of ozone pollution in eastern Chinese cities applying convolutional neural network*, *J. Environ. Sci. (China)* **148**, 126 (2024). <https://doi.org/10.1016/j.jes.2023.09.001>.
25. Y. Huang, P. Wang, Z. Yang, P. Yu, T. Ye, Y. Guo, and L. Huang, *Spatiotemporal characteristics and influencing factors for joint events of air pollution wave and cold wave in China*, *Environ. Int.* **184**, 108475 (2024). <https://doi.org/10.1016/j.envint.2024.108475>.
26. J. Xiong, J. Li, Y. Zhang, and G. Mao, *Meteorological Impact on Dynamic Air Pollutant Concentrations in Different Timescales: Typical Case in Chengdu Megacity, China*, *Water, Air, Soil Pollut.* **234**, 688 (2023). <https://doi.org/10.1007/s11270-023-06711-z>.
27. S. Wu, X. Yan, J. Yao, and W. Zhao, *Quantifying the scale-dependent relationships of PM_{2.5} and O₃ on meteorological factors and their influencing factors in the Beijing-Tianjin-Hebei region and surrounding areas*, *Environ. Pollut.* **337**, 122517 (2023). <https://doi.org/10.1016/j.envpol.2023.122517>.
28. A. Ajdour, R. Leghrib, J. Chaoufi, and A. Chirmata, *High spatial resolution effect on ozone pollution modelling: Case study of Agadir city (Morocco)*, *Mater. Today Proc.* **52**, 137 (2022). <https://doi.org/10.1016/j.matpr.2021.11.278>.
29. A. Riccio and E. Chianese, *Technical note: Accurate, reliable, and high-resolution air quality predictions by improving the Copernicus Atmosphere Monitoring Service using a novel statistical post-processing method*, *Atmos. Chem. Phys.* **24**, 1673 (2024). <https://doi.org/10.5194/acp-24-1673-2024>.
30. Z. Elouaourti and E. Ezzahid, *Factors of regional financial inclusion in Morocco*, *Reg. Sci. Policy Pract.* **16**, 12516 (2022). <https://doi.org/10.1111/rsp3.12516>.

31. O. N. Mensour, B. El Ghazzani, B. Hlimi, and A. Ihlal, *A geographical information system-based multi-criteria method for the evaluation of solar farms locations: A case study in Souss-Massa area, southern Morocco*, *Energy* **182**, 900 (2019). <https://doi.org/10.1016/j.energy.2019.06.063>.
32. Y. Almulla, C. Ramirez, B. Joyce, A. Huber-Lee, and F. Fuso-Nerini, *From participatory process to robust decision-making: An Agriculture-water-energy nexus analysis for the Souss-Massa basin in Morocco*, *Energy Sustain. Dev.* **70**, 314 (2022). <https://doi.org/10.1016/j.esd.2022.08.009>.
33. S. Afyouni, S. M. Smith, and T. E. Nichols, *Effective degrees of freedom of the Pearson's correlation coefficient under autocorrelation*, *Neuroimage* **199**, 609 (2019). <https://doi.org/10.1016/j.neuroimage.2019.05.011>.
34. E. Saccenti, M. H. W. B. Hendriks, and A. K. Smilde, *Corruption of the Pearson correlation coefficient by measurement error and its estimation, bias, and correction under different error models*, *Sci. Rep.* **10**, 1 (2020). <https://doi.org/10.1038/s41598-019-57247-4>.
35. U. Mueller, *Multiple Correlation Coefficient*, *Encycl. Math. Geosci.* **1**, pp. 1–3 (2020). https://doi.org/10.1007/978-3-030-26050-7_221-1.
36. M. N. Murshed and M. M. Uddin, *Towards an Adaptive Dynamic Mode Decomposition*, *Results Control Optim.* **6**, 100076 (2022). <https://doi.org/10.1016/j.rico.2021.100076>.
37. M. Greenacre, *Compositional data analysis*, *Annu. Rev. Stat. Its Appl.* **8**, 271 (2021). <https://doi.org/10.1146/annurev-statistics-042720-124436>.
38. S. R. Shams, A. Jahani, S. Kalantary, M. Moeinaddini, and N. Khorasani, *The evaluation on artificial neural networks (ANN) and multiple linear regressions (MLR) models for predicting SO2 concentration*, *Urban Clim.* **37**, 100837 (2021). <https://doi.org/10.1016/j.uclim.2021.100837>.
39. G. James, D. Witten, T. Hastie, R. Tibshirani, and J. Taylor, *Linear Regression*, *Intro Stat Learn.* **1**, pp. 69–134 (2023). https://doi.org/10.1007/978-3-031-38747-0_3.
40. A. C. Cinar and N. Natarajan, *An artificial neural network optimized by grey wolf optimizer for prediction of hourly wind speed in Tamil Nadu, India*, *Intell. Syst. with Appl.* **16**, 200138 (2022). <https://doi.org/10.1016/j.iswa.2022.200138>.
41. Z. Sabir, M. R. Ali, M. A. Z. Raja, M. Shoaib, R. A. S. Núñez, and R. Sadat, *Correction to: Computational intelligence approach using Levenberg–Marquardt backpropagation neural networks to solve the fourth-order nonlinear system of Emden–Fowler model*, *Eng. Comput.* **38**, 2993 (2022). <https://doi.org/10.1007/s00366-022-01652-3>.
42. Q. H. Nguyen, H. B. Ly, L. S. Ho, N. Al-Ansari, H. Van Le, V. Q. Tran, I. Prakash, and B. T. Pham, *Influence of data splitting on performance of machine learning models in prediction of shear strength of soil*, *Math. Probl. Eng.* **2021**, (2021). <https://doi.org/10.1155/2021/4832864>.
43. Y. Ma and G. Guo, *Intelligent algorithm of geotechnical test data based on Internet of Things*, *Comput. Commun.* **158**, 32 (2020). <https://doi.org/10.1016/j.comcom.2020.04.028>.
44. J. Aminov, G. Dupont-Nivet, D. Ruiz, and B. Gailleton, *Paleogeographic reconstructions using QGIS: Introducing Terra Antiqua plugin and its application to 30 and 50 Ma maps*, *Earth-Science Rev.* **240**, 104401 (2023). <https://doi.org/10.1016/j.earscirev.2023.104401>.
45. A. J. Garner and D. P. Duran, *Late-Winter and Springtime Temperature Variations throughout New Jersey in a Warming Climate*, *J. Appl. Meteorol. Climatol.* (2023). <https://doi.org/10.1175/jamc-d-23-0152.1>.
46. A. Chirmata, R. Leghrib, and I. A. Ichou, *Implementation of the Air Quality Monitoring Network at Agadir City in Morocco*, *J. Environ. Prot. (Irvine, Calif.)* **08**, 540 (2017). <https://doi.org/10.4236/jep.2017.84037>.
47. F. Dettner and M. Blohm, *External cost of air pollution from energy generation in Morocco*, *Renew. Sustain. Energy Transit.* **1**, 100002 (2021). <https://doi.org/10.1016/j.rset.2021.100002>.
48. X. Meng, J. Jiang, T. Chen, Z. Zhang, B. Lu, C. Liu, L. Xue, J. Chen, H. Herrmann, and X. Li, *Chemical drivers of ozone change in extreme temperatures in eastern China*, *Sci. Total Environ.* **874**, 162424 (2023). <https://doi.org/10.1016/j.scitotenv.2023.162424>.

49. N. R. Awang, N. A. Ramli, S. Shith, N. S. Zainordin, and H. Manogaran, *Transformational characteristics of ground-level ozone during high particulate events in urban area of Malaysia*, *Air Qual. Atmos. Heal.* **11**, 715 (2018). <https://doi.org/10.1007/s11869-018-0578-0>.
50. F. Cifuentes, A. Gálvez, C. M. González, M. Orozco-Alzate, and B. H. Aristizábal, *Hourly ozone and pm2.5 prediction using meteorological data – alternatives for cities with limited pollutant information*, *Aerosol Air Qual. Res.* **21**, (2021). <https://doi.org/10.4209/aaqr.200471>.
51. B. Bera, S. Bhattacharjee, N. Sengupta, and S. Saha, *Variation and dispersal of PM10 and PM2.5 during COVID-19 lockdown over Kolkata metropolitan city, India investigated through HYSPLIT model*, *Geosci. Front.* **13**, 101291 (2022). <https://doi.org/10.1016/j.gsf.2021.101291>.
52. T. Miyama, H. Matsui, K. Azuma, C. Minejima, Y. Itano, N. Takenaka, and M. Ohyama, *Time series analysis of climate and air pollution factors associated with atmospheric nitrogen dioxide concentration in Japan*, *Int. J. Environ. Res. Public Health* **17**, 1 (2020). <https://doi.org/10.3390/ijerph17249507>.
53. Y. Yue, J. Cheng, K. S. Lee, R. Stocker, X. He, M. Yao, and J. Wang, *Effects of relative humidity on heterogeneous reaction of SO2 with CaCO3 particles and formation of CaSO4·2H2O crystal as secondary aerosol*, *Atmos. Environ.* **268**, (2022). <https://doi.org/10.1016/j.atmosenv.2021.118776>.
54. M. Khalis, A. B. Toure, I. El Badisy, K. Khomsi, H. Najmi, O. Bouaddi, A. Marfak, W. K. Al-Delaimy, M. Berraho, and C. Nejjari, *Relationship between Meteorological and Air Quality Parameters and COVID-19 in Casablanca Region, Morocco*, *Int. J. Environ. Res. Public Health* **19**, (2022). <https://doi.org/10.3390/ijerph19094989>.
55. A. Rathore, G. S. Gopikrishnan, and J. Kuttippurath, *Changes in tropospheric ozone over India: Variability, long-term trends and climate forcing*, *Atmos. Environ.* **309**, 119959 (2023). <https://doi.org/10.1016/j.atmosenv.2023.119959>.
56. D. H. Nguyen, C. Lin, C. T. Vu, N. K. Cheruiyot, M. K. Nguyen, T. H. Le, W. Lukkhasorn, T. D. H. Vo, and X. T. Bui, *Tropospheric ozone and NOx: A review of worldwide variation and meteorological influences*, *Environ. Technol. Innov.* **28**, (2022). <https://doi.org/10.1016/j.eti.2022.102809>.
57. N. G. Birim, C. Turhan, A. S. Atalay, and G. Gokcen Akkurt, *The Influence of Meteorological Parameters on PM10: A Statistical Analysis of an Urban and Rural Environment in Izmir/Türkiye*, *Atmosphere (Basel)*. **14**, (2023). <https://doi.org/10.3390/atmos14030421>.
58. T. Ju, T. Geng, B. Li, B. An, R. Huang, J. Fan, Z. Liang, and J. Duan, *Impacts of Certain Meteorological Factors on Atmospheric NO2 Concentrations during COVID-19 Lockdown in 2020 in Wuhan, China*, *Sustain.* **14**, (2022). <https://doi.org/10.3390/su142416720>.
59. J. Cao, X. Qiu, J. Gao, F. Wang, J. Wang, J. Wu, and L. Peng, *Significant decrease in SO2 emission and enhanced atmospheric oxidation trigger changes in sulfate formation pathways in China during 2008–2016*, *J. Clean. Prod.* **326**, 129396 (2021). <https://doi.org/10.1016/j.jclepro.2021.129396>.
60. Z. Kazi, S. Filip, and L. Kazi, *Predicting PM2.5, PM10, SO2, NO2, NO and CO Air Pollutant Values with Linear Regression in R Language*, *Appl. Sci.* **13**, (2023). <https://doi.org/10.3390/app13063617>.
61. L. P. S. Cruz, E. R. Mota, V. P. Campos, F. O. Santana, S. R. Luz, and D. F. Santos, *Inorganic and organic acids in the atmosphere of the urban area of the city of Salvador, Brazil*, *J. Braz. Chem. Soc.* **30**, 904 (2019). <https://doi.org/10.21577/0103-5053.20180227>.
62. Z. Wang et al., *Characterizing nighttime vertical profiles of atmospheric particulate matter and ozone in a megacity of south China using unmanned aerial vehicle measurements*, *Environ. Res.* **236**, 116854 (2023). <https://doi.org/10.1016/j.envres.2023.116854>.
63. Y. You, X. Wang, Y. Wu, W. Chen, B. Chen, and M. Chang, *Quantified the influence of different synoptic weather patterns on the transport and local production processes of O3 events in Pearl River Delta, China*, *Sci. Total Environ.* **912**, 169066 (2024). <https://doi.org/10.1016/j.scitotenv.2023.169066>.

64. J. Du, F. Qiao, P. Lu, and L. Yu, *Forecasting ground-level ozone concentration levels using machine learning*, *Resour. Conserv. Recycl.* **184**, 106380 (2022). <https://doi.org/10.1016/j.resconrec.2022.106380>.
65. Y. Li, S. S. Dhomse, M. P. Chipperfield, W. Feng, J. Bian, Y. Xia, and D. Guo, *Quantifying stratospheric ozone trends over 1984-2020: a comparison of ordinary and regularized multivariate regression models*, *Atmos. Chem. Phys.* **23**, 13029 (2023). <https://doi.org/10.5194/acp-23-13029-2023>.
66. Y. Cheng, Q. Zhu, Y. Peng, X. F. Huang, and L. Y. He, *Multiple strategies for a novel hybrid forecasting algorithm of ozone based on data-driven models*, *J. Clean. Prod.* **326**, 129451 (2021). <https://doi.org/10.1016/j.jclepro.2021.129451>.
67. A. Al Yammani and Z. Aung, *Forecasting the concentration of NO₂ using statistical and machine learning methods: A case study in the UAE*, *Heliyon* **9**, e12584 (2023). <https://doi.org/10.1016/j.heliyon.2022.e12584>.
68. C. Huang, K. Sun, J. Hu, T. Xue, H. Xu, and M. Wang, *Estimating 2013–2019 NO₂ exposure with high spatiotemporal resolution in China using an ensemble model*, *Environ. Pollut.* **292**, 118285 (2022). <https://doi.org/10.1016/j.envpol.2021.118285>.
69. A. Sayeed, Y. Lops, Y. Choi, J. Jung, and A. K. Salman, *Bias correcting and extending the PM forecast by CMAQ up to 7 days using deep convolutional neural networks*, *Atmos. Environ.* **253**, 118376 (2021). <https://doi.org/10.1016/j.atmosenv.2021.118376>.
70. A. S. Jesemann, V. Matthias, J. Böhner, and B. Bechtel, *Using Neural Network NO₂-Predictions to Understand Air Quality Changes in Urban Areas—A Case Study in Hamburg*, *Atmosphere (Basel)*, **13**, (2022). <https://doi.org/10.3390/atmos13111929>.
71. C. Tao, M. Jia, G. Wang, Y. Zhang, Q. Zhang, X. Wang, Q. Wang, and W. Wang, *Time-sensitive prediction of NO₂ concentration in china using an ensemble machine learning model from multi-source data*, *J. Environ. Sci. (China)* **137**, 30 (2024). <https://doi.org/10.1016/j.jes.2023.02.026>.
72. P. Schober and L. A. Schwarte, *Correlation coefficients: Appropriate use and interpretation*, *Anesth. Analg.* **126**, 1763 (2018). <https://doi.org/10.1213/ANE.0000000000002864>.
73. R. le Roux, S. Henrico, J. Bezuidenhout, and I. Henrico, *Inverse Distance Weighting as an alternative interpolation method to create radiometric maps of natural radionuclide concentrations using QGIS*, *Proc. ICA* **5**, 1 (2023). <https://doi.org/10.5194/ica-proc-5-10-2023>.
74. L. Salgado, C. A. López-Sánchez, A. Colina, D. Baragaño, R. Forján, and J. R. Gallego, *Hg and As pollution in the soil-plant system evaluated by combining multispectral UAV-RS, geochemical survey and machine learning*, *Environ. Pollut.* **333**, (2023). <https://doi.org/10.1016/j.envpol.2023.122066>.
75. Y. H. Ryu and S. K. Min, *Long-term evaluation of atmospheric composition reanalyses from CAMS, TCR-2, and MERRA-2 over South Korea: Insights into applications, implications, and limitations*, *Atmos. Environ.* **246**, 118062 (2021). <https://doi.org/10.1016/j.atmosenv.2020.118062>.
76. D. B. Lobell, S. Di Tommaso, and J. A. Burney, *Globally ubiquitous negative effects of nitrogen dioxide on crop growth*, *Sci. Adv.* **8**, 1 (2022). <https://doi.org/10.1126/sciadv.abm9909>.
77. P. Aszkowski, B. Ptak, M. Kraft, D. Pieczyński, and P. Drapikowski, *Deepness: Deep neural remote sensing plugin for QGIS*, *SoftwareX* **23**, 101495 (2023). <https://doi.org/10.1016/j.softx.2023.101495>.
78. Regional Directorate of the High Commission for Planning, *Agadir and Inzegane Ait Melloul Prefectures In Figures 2020, 2019 (2020)*. [https://www.hcp.ma/region-agadir/docs/docs/Agadir Ida Outanane en chiffres 2021.pdf](https://www.hcp.ma/region-agadir/docs/docs/Agadir%20Outanane%20en%20chiffres%202021.pdf).